A walnut shell biochar-nano zero-valent iron composite membrane for the degradation of carbamazepine via persulfate activation

Yongtao Xue [a], Mohammadreza Kamali [a], Alina Liyakat [a], Maud Bruggeman [a], Zeeshan Muhammad [a], Barbara Rossi [b], Maria Elisabete V. Costa [c], Lise Appels [a], Raf Dewil [a, b, *]

[a] KU Leuven, Department of Chemical Engineering, Process and Environmental Technology Lab, J. De Nayerlaan 5, 2860 Sint-Katelijne-Waver, Belgium

[b] University of Oxford, Department of Engineering Science, Parks Road, Oxford OX1 3PJ, United Kingdom

[c] University of Aveiro, Department of Materials and Ceramics Engineering, Aveiro Institute of Materials, CICECO, 3810-193, Aveiro, Portugal

* corresponding author: raf.dewil@kuleuven.be (R. Dewil)

Abstract: In this study, novel walnut shell biochar-nano zero-valent iron nanocomposites (WSBC-nZVI) were synthesized using a combined pyrolysis/reduction process. WSBC-nZVI displayed a high removal efficiency (86%) for carbamazepine (CBZ) compared with walnut shell biochar (70%) and nano zero-valent iron (76%) in the presence of persulfate (PS) (0.5 g/L catalyst, 10 mg/L CBZ, 1 mM persulfate). Subsequently, WSBC-nZVI was applied for the fabrication of the membrane using a phase inversion method. The membrane demonstrated an excellent removal efficiency of 91% for CBZ in a dead-end system (2 mg/L CBZ, 1 mM persulfate). In addition, the effect of various operating conditions on the degradation efficiency in the membrane/persulfate system was investigated. The optimum pH was close to neutral, and an increase in CBZ concentration from 1 mg/L to 10 mg/L led to a drop in removal efficiency from 100% to 24%. The degradation mechanisms indicated that oxidative species, including $^1O_2$, ·OH, $SO_4^{\cdot-}$, and $O_2^{\cdot-}$, all contribute to the degradation of CBZ, while the role of $^1O_2$ is highlighted. The CBZ degradation products were also investigated, and the possible pathways and the predicted toxicity of intermediates were proposed. Furthermore, the practical use of the membrane was validated by the treatment of real wastewater.

Keywords: walnut shell biochar; nano zero-valent iron; catalytic membrane; persulfate; mechanisms.

1. Introduction

Carbamazepine (CBZ), as a typical anticonvulsant drug, is widely used to cure mental illnesses such as epilepsy (Roy and Moholkar, 2021; Zybina et al., 2018). CBZ is a polar molecule and relatively stable, has a low degree of volatility, and will hence accumulate in various water bodies (i.e., surface water, drinking water, and ground water) because of the ineffectiveness of conventional wastewater treatment methods (e.g., activated sludge process) to remove this pharmaceutically active compound (Fan et al., 2020; H. Zhou et al., 2020). According to the literature, CBZ can cause short-term and long-term toxic effects to living organisms, such as endocrine disruption and teratogenicity (Su et al., 2022). To address these issues, various physicochemical methods have been developed for the treatment of CBZ-containing wastewater. Some cost-effective methods, such as adsorption, have already demonstrated acceptable removal efficiencies for CBZ (e.g., a high adsorption capacity of 664 mg/g with Zn-MOF-derived nanoporous carbons (Yu et al., 2022)). However, the treatment of spent adsorbents is a challenging issue and may cause secondary pollution (Wen et al., 2019). Various advanced oxidation processes have been considered for the removal of CBZ. Among these methods, electrochemical methods are able to generate strong oxidation species for the degradation of contaminants but require expensive facilities and large amounts of energy input, which can limit their commercialization for real applications (Tang et al., 2019). Activation of oxidation agents such as hydrogen peroxide, persulfate, and iodine is another way of dealing with such recalcitrant pollutants by generating powerful oxidative species in the medium. In this regard, sulfate radicals with a high oxidation potential (2.5-3.1 V), and long half-life period (30-40 μs) (Luo et al., 2018) have recently received great attention, leading to the development of various homogeneous (e.g., using microwaves (Qi et al., 2014), heating (Liu et al., 2023), and ultrasound (Monteagudo et al., 2018)) and heterogeneous (e.g., using catalysts) persulfate activation techniques. Among them, heterogeneous catalytic systems using transition metals have been considered good candidates for the activation of PS due to their high degradation efficiency and high feasibility. In particular,

nano zero-valent iron (nZVI) has been widely applied for the activation of PS, mainly because of its effective redox chemistry properties and non-toxic nature (Chen et al., 2018). However, nZVI suffers from aggregation and passivation, which cause the loss of effective surface area and reduce its efficiency for the degradation of pollutants, resulting in restricted application for the treatment of real wastewater (Shan et al., 2021). Several methods have been developed to overcome this barrier, including the addition of surfactants (e.g., sodium dodecyl) (Wang et al., 2021), second metal doping (Wu et al., 2022), and using a support to stabilize the iron particles (Fan et al., 2022). Among these methods, the use of carbonaceous materials to support nZVI has received huge attention because they provide abundant surface functional groups, high porosity and high specific surface area at relatively low costs, which meet economic and environmental requirements (Xue et al., 2023). In addition, carbonaceous material-supported nZVI displays high stability and excellent degradation performance for a wide range of pollutants. For instance, Li et al. (Li et al., 2022) synthesized nZVI/N-doped biochar for the degradation of bisphenol A (BPA) in the presence of peroxydisulfate, and the composites displayed a high degradation efficiency of 95% in 120 min. Biochar (BC), as a typical carbonaceous material, is generally produced through the pyrolysis of biomass feedstocks under oxygen-limited conditions (Li et al., 2021). BC is considered an effective support material for the immobilization of nZVI, especially when it has a high specific surface area and porosity resulting from the optimum pyrolysis process (Xu et al., 2018). Nevertheless, the rapid agglomeration and issues related to the recycling of spent composite nanomaterials are challenging aspects related to their industrial application (Xue et al., 2022b). To overcome these issues, catalytic membrane processes for the treatment of wastewater have been studied and developed rapidly in recent years. In such advanced systems, the membrane not only separates suspended solids but also degrades organic pollutants using immobilized nanomaterials. For instance, Liu et al. (Liu et al., 2021) fabricated a CuO@CuS/PVDF composite membrane for the degradation of tetracycline, resulting in a high removal efficiency of 87% within 3 h in the presence of persulfate. Inspired by this, the

construction of a BC-nZVI membrane represents some advantages, including strong stability, easy recovery, environmental friendliness, and high efficiency.

In the present manuscript, walnut shell biochar (WSBC)-supported nZVI was synthesized through a combined pyrolysis/reduction process. Subsequently, a WSBC-nZVI membrane was fabricated via phase inversion for the activation of PS. To the best of our knowledge, there is no report in the literature about the fabrication of a walnut shell biochar-nano zero-valent iron (WSBC-nZVI) membrane and its use for the activation of PS. In addition, the effect of different operating conditions (such as PS concentration, solution pH, and CBZ concentration) on CBZ degradation in the WSBC-nZVI membrane/PS system was determined, and optimal conditions were defined. The involved mechanisms were investigated by scavenging experiments, and the feasibility of this system was examined for the treatment of real wastewater. Furthermore, the degradation products and proposed degradation pathways of CBZ were studied. Finally, the stability of the membrane was evaluated.

2. Materials and method

2.1 Chemicals

Chemicals including iron(II)-sulfate heptahydrate ($FeSO_4 \cdot 7H_2O$, ACS reagent, >99,5%, Carl Roth, Germany), sodium borohydride ($NaBH_4$, ACS reagent, 98%, Fischer Scientific, Germany), sodium persulfate ($Na_2S_2O_8$, ACS reagent, Belgium), polyethylene glycol (PEG 2000, Fischer Scientific, Germany), polyethersulfone (PES, 6020p, western union, China), N,N-dimethylformamide (DMF, C_3H_7NO, ACS reagent, >= 99,8%, Thermo Scientific, Turkey), carbamazepine ($C_{15}H_{12}N_2O$, Sigma-Aldrich, Germany), acetonitrile (ACN, HPLC grade, Fisher Chemical, UK), and formic acid (FA, HPLC grade, Honeywell, Germany) were used during the experiments.

2.2 Synthesis of nanomaterials

Walnut shell particulate material was obtained from Matthys bvba (Belgium) with a particle size ranging from 450 µm to 800 µm. For the preparation of walnut shell biochar, 20 g of walnut

shell was impregnated with 100 mL of H_3PO_4 (0.6 M) at 90 °C for 3 h and then dried at 80 °C overnight. This pre-treatment step enhances the porosity of the fabricated materials, as previously reported by Chen et al. (Chen et al., 2022). Subsequently, the obtained material was pyrolysed at 520 °C with a heating rate of 10 °C/min and held at 520 °C for 2 h. The pyrolysis process was carried out under a nitrogen atmosphere. The prepared biochar was collected and labelled WSBC for further characterization and use.

WSBC-nZVI was synthesized using a liquid phase reduction process. WSBC (0.4 g) and $FeSO_4{\cdot}7H_2O$ (6 g) were dispersed in 400 mL distilled water under stirring and a nitrogen atmosphere for 30 min. Then, 200 mL $NaBH_4$ solution with a concentration of 20 g/L was added dropwise into the mixture with flowing nitrogen. After 1 h of reaction, the WSBC-nZVI powder was collected and washed with distilled water three times. Finally, the WSBC-nZVI was dried at 60 °C overnight under a nitrogen atmosphere. nZVI was also synthesized through the same method without WSBC.

2.3 Fabrication of WSBC-nZVI membrane

The WSBC-nZVI membrane was fabricated through a phase inversion method. The WSBC-nZVI nanomaterial (2%) was dispersed into a DMF solution (70%) and then distributed uniformly under ultrasound conditions for 30 min. Subsequently, PES (16%) and PEG (12%) were added to the above solution. The mixture was heated at 60 °C for 6 h under continuous stirring. The obtained homogenous solution was degassed by ultrasound for 30 min to remove any bubbles from the solution. Then, the solution was evenly spread onto a glass plate using a casting knife (Elcometer 3580, Netherlands) to set a wet membrane thickness of 200 μm. Thereafter, the glass plate was immediately immersed in a distilled water bath at room temperature until the membrane spontaneously detached from the glass plate. The membrane was stored in distilled water under a N_2 atmosphere to remove the residual organic solvent.

2.4 Characterization

The composition and crystalline structure of the prepared nanomaterials were studied by using X-ray diffraction analysis (XRD, Panalytical X'Pert PRO 3, Netherlands). The surface functional groups of the prepared nanomaterials and membrane were also identified via Fourier transform infrared spectroscopy (FTIR) using an attenuated total reflection (ATR) diamond accessory (FTIR-ATR, Bruker). In addition, the morphology and elemental composition of the prepared nanomaterials and membrane were also characterized by using scanning electron microscopy (SEM) with energy dispersive spectroscopy (EDS) (VEGA3 TESCAN). Nitrogen adsorption-desorption isotherms were obtained using a Micromeritics Gemini V2 (USA) to identify the specific surface area and pore size distribution of the prepared materials.

2.5 Degradation of CBZ

CBZ degradation experiments with the prepared nanomaterials were carried out in a beaker at room temperature. Typically, 0.5 g/L nanomaterials and 1 mM PS were added to 200 mL CBZ solution (10 mg/L) under continuous stirring. At fixed time intervals, approximately 1.5 mL of suspension was sampled, filtered by a 0.45 μm filter and quenched by $Na_2S_2O_3$ solution. The concentrations of CBZ were measured by high-performance liquid chromatography (HPLC). A C18 column (Agilent Eclipse Plus, 4.6 × 250 mm, dp= 5 μm) was used at 30 °C. The mobile phase consisted of water and ACN with a ratio of 60:40 (v/v), and the UV detector was set at 284 nm. The sample injection volume was 30 μL. The degradation efficiency and degradation reaction rate constant of CBZ were calculated according to Equations (1) and (2).

$$\text{Degradation efficiency (\%)} = 100 \times (C_0 - C_t)/C_0 \quad (1)$$

$$ln\,(C_t/C_0) = -K_{obs} \times t \quad (2)$$

where C_0 is the initial CBZ concentration (mg/L) and C_t is the CBZ concentration at reaction time (t). K_{obs} is the pseudo-first-order reaction rate constant (min^{-1}).

The WSBC-nZVI catalytic membrane performance for CBZ degradation was investigated in a dead-end filtration setup (Memtester, Switzerland). A fresh membrane (storage time less than 24

h) with an effective area of 28 cm^2 was placed in a stirred cell. Subsequently, 200 mL of CBZ solution and 1 mM PS were mixed in the filtration cell with a total volume of 300 mL under continuous stirring (air not evacuated). Then, a constant pressure of 0.5 bar was provided by a nitrogen gas bottle. At pre-determined time intervals, a 1.5 mL sample of the permeate aqueous solution was collected and quenched by the $Na_2S_2O_3$ solution to stop the oxidation reactions. The pH of the solution was adjusted by 0.1 M HNO_3 or 0.1 M NaOH if needed. The concentration of CBZ was measured using the method described in section 2.5. In addition, the water permeability of the membrane was calculated using Equation (3) (Zheng et al., 2022).

$$\text{Water permeability} = V/(A \cdot t \cdot P) \quad (3)$$

where V (L) is the volume of the permeated solution, A (m^2) is the effective area of the membrane, t (h) is the filtration time, and P (bar) is the operating pressure. Moreover, the catalytic performance of the membrane for real wastewater was studied in the same way, using real wastewater instead of Milli-Q water. The reuse experiment was also carried out with the spent membrane and by feeding the system CBZ-polluted water and PS.

The degradation products of CBZ were identified by an Agilent Infinity II 1290 UHPLC/DAD instrument coupled to a quadrupole time-of-flight mass spectrometer (Q-TOF MS) (Agilent 6530, Waldbronn, Germany). Two Acquity UPLC BEH C18 columns (2.1 × 100 mm, dp 1.7 μm, Waters, Milford, USA) were connected in series and operated at a flow rate of 0.25 mL/min. The mobile phases included 0.1% FA in water (A) and 0.1% FA in acetonitrile (B). A gradient elution method was carried out as follows: 10% B to 31.25% B in 0-5 min, 31.25% B to 95% B in 5-30 min, kept for 2 min, 95% B to 10% B in 32-33 min, reconditioned for 12 min at 10% B. Positive electrospray ionization mode (ESI^+) was used. The gas temperature, sheath gas temperature, sheath gas flow, drying gas flow, and capillary voltage were 315 °C, 350 °C, 660 L/h, 480 L/h, and 3.5 kV, respectively. The mass scan range was from m/z 50 to m/z 1700. Agilent Profinder software (version 10.0) was utilized to analyse the data.

3. Results and discussion

3.1 Characterization of the nanomaterials and membrane

The crystal structure of the prepared materials was analysed by XRD, and Fig. 1 presents the results obtained. WSBC displays an obvious peak at approximately 24°, which can be attributed to the amorphous structure of carbon (X. Zhou et al., 2020). The characteristic peak at 44.7 ° of nZVI matches well with the standard patterns of Fe^0 (JCPDS 06-0696) (Li et al., 2020). In addition, the small peak at approximately 35° of nZVI is related to the partial oxidation of nZVI. The intensity of this peak decreased obviously in WSBC-nZVI, revealing that WSBC protects nZVI particles from further oxidation. This may be because a portion of nZVI can be synthesized in the pores of BC; hence, BC may mechanically prevent nZVI from interacting with air (Han et al., 2015). Similar results have been reported by Gu et al. (Gu et al., 2021). They found that the presence of BC and graphene in a composite prevents the oxidation of nZVI. In addition, WSBC-nZVI exhibits the characteristic peaks of nZVI, while the amorphous peak of WSBC at 24° disappears after the addition of nZVI.

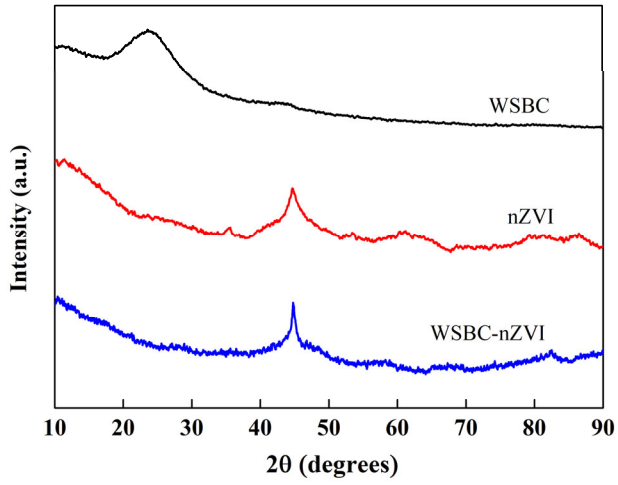

Fig. 1
XRD patterns of WSBC, nZVI, and WSBC-nZVI.

The surface functional groups of the prepared nanomaterials and membranes were also identified using FTIR spectroscopy. The characteristic peaks of WSBC at 2103 cm^{-1}, 1692 cm^{-1}, 1550 cm^{-1}, 1090 cm^{-1}, 680 cm^{-1}, and 462 cm^{-1} shown in Fig. 2a are related to the vibrations of C≡C,

-COOH vibration, bending vibration of N-H, stretching vibration of C-O, C-H deformation, and bending and symmetrical vibration of Si-O-Si, respectively (Boguta et al., 2019; Soria et al., 2020; Xiao et al., 2020; Yang et al., 2022). In addition, WSBC-nZVI retains the original characteristic peaks of WSBC, indicating that the WSBC-nZVI nanocomposite has been successfully synthesized. It has been reported that the abundant surface functional groups of nanomaterials play a key role in the adsorption and degradation of contaminants (Ahmad et al., 2020). For instance, Silvestri et al. (Silvestri et al., 2021) found that surface functional groups such as carbonyl groups can boost the activation of PS for the degradation of contaminants, which can be attributed to the fact that carbonyl groups, as the main active sites of BC, contribute to electron transfer between pollutants and PS. The characteristic peaks of PES at 1578 cm^{-1}, 1486 cm^{-1}, 1236, and 1103 cm^{-1} (Fig. 2b) are associated with C=C aromatic ring vibration, C–C stretching, aromatic phenylene ether stretching, and C–O stretching, respectively (Heng et al., 2021). Additionally, PEG presents several characteristic peaks, such as 2870 cm^{-1} and 1104 cm^{-1}, which can be attributed to CH_2 asymmetric stretching and -C-O- vibrations, respectively (Dilshad et al., 2019). Moreover, the WSBC-nZVI membrane demonstrates several characteristic peaks for PES (e.g., 1578 cm^{-1}) and PEG (e.g., 2870 cm^{-1}), but no obvious characteristic peaks of WSBC-nZVI are observed. This can be attributed to the fact that the high-intensity peaks of PES and PEG (e.g., 1578 cm^{-1}, 1236 cm^{-1}, 1103 cm^{-1}) affect the characteristic peaks of nanomaterials (e.g., 1090 cm^{-1}, 680 cm^{-1}) in the same region, resulting in the characteristic peaks of WSBC-nZVI being undistinguishable.

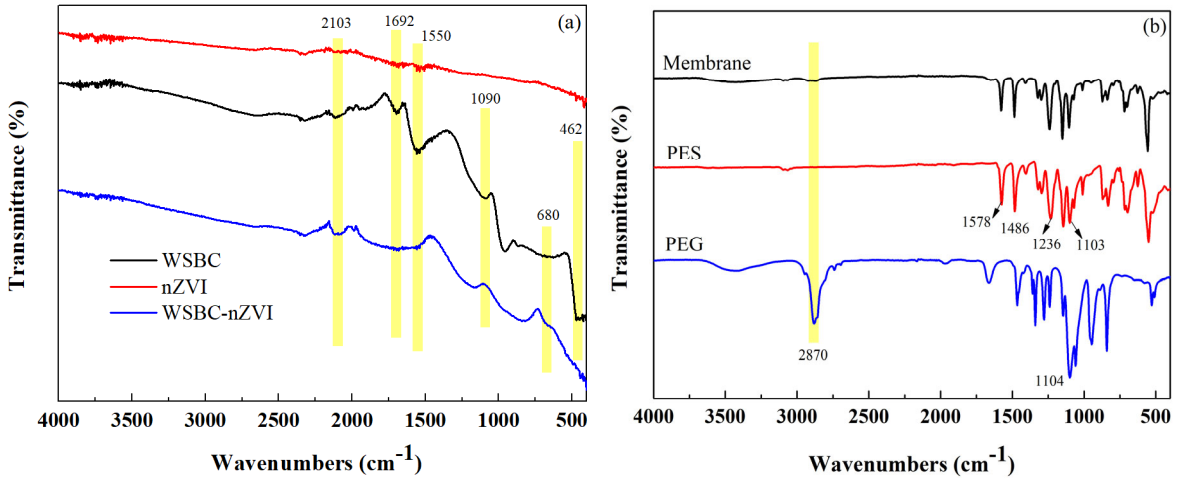

Fig. 2
FTIR spectra of the prepared WSBC, nZVI, and WSBC-nZVI nanomaterials (a), PES, PEG, and WSBC-nZVI membrane (b).

The morphology and elemental composition of the prepared nanomaterials and the membrane were analysed using SEM and mapping techniques. Fig. 3a demonstrates the vesicle-type morphology of WSBC with a porous structure. nZVI presents as agglomerated spherical particles. The aggregation of nanosized particles is due to the van der Waals interactions between nanosized magnetic particles (Li et al., 2019). Mandal et al. (Mandal et al., 2020) also observed that nZVI had non-uniform and agglomerated spherical structure shapes. In Fig. 3d-e, the morphology of WSBC-nZVI clearly confirms that the nZVI particles are well dispersed at the surface and pores of WSBC. In addition, the mapping of WSBC-nZVI proves the presence of C, O, and Fe in the materials, as indicated in Fig. 3e-i. Furthermore, the presence of WSBC-nZVI particles on the surface of the membrane is evident from Fig. 3j. The cross-sectional images of the membrane (Fig. 3 k-m) also reveal its porous and spongy morphology. The formation of porous structures is due to the use of PEG as a pore-forming agent in the membrane fabrication process. In addition, the presence of hydrophilic oxygen-containing groups (such as -COOH and C-O, Fig. 2) on the surface of WSBC-nZVI nanoparticles can improve the diffusion rate of water into the membrane during the fabrication process of the membrane, which results in the formation and development of pores. Similar results have been reported by He et al. (He et al., 2017). They concluded that the presence

of BC can considerably enhance the porosity of the membrane compared to the pristine membrane without BC (79%>75%).

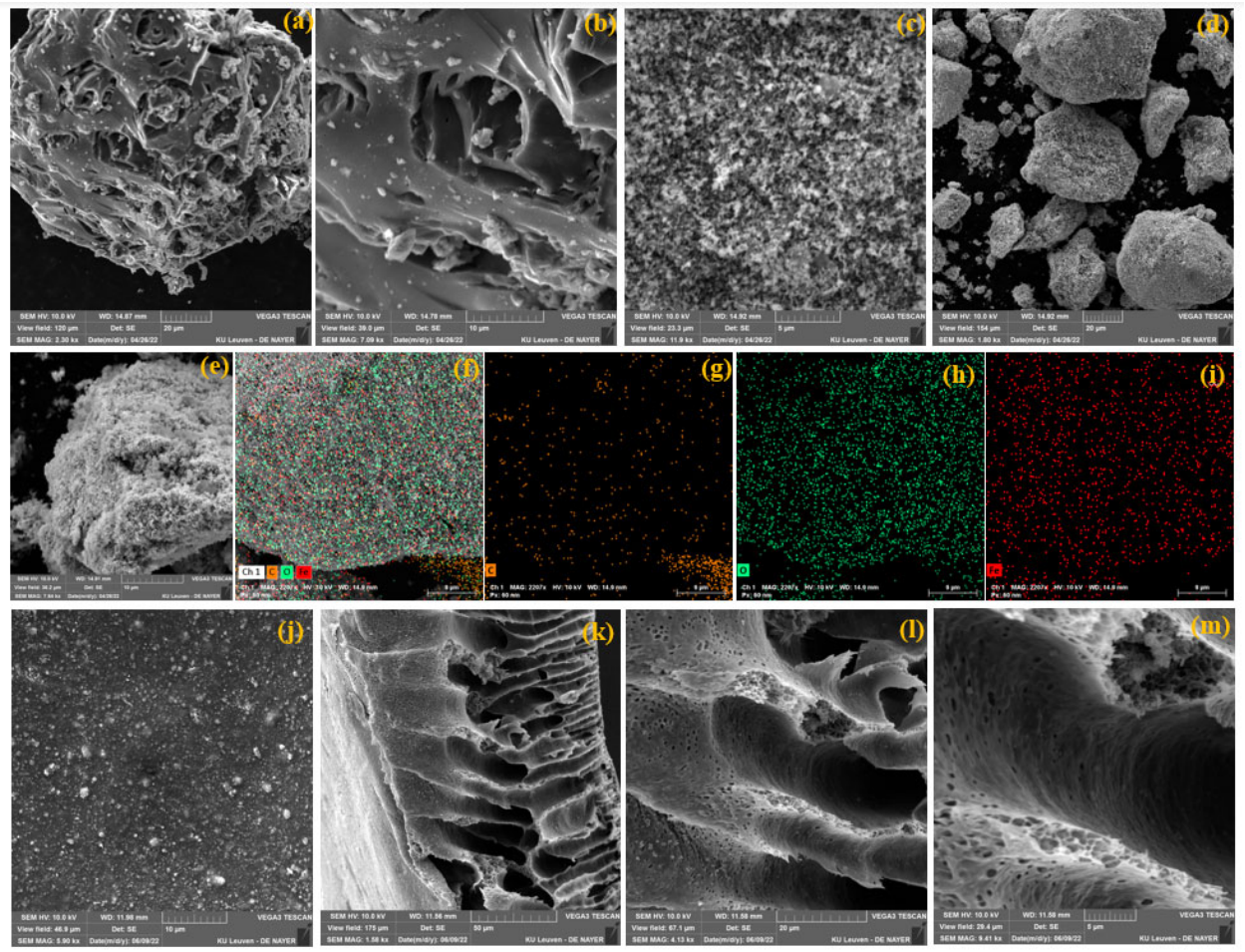

Fig. 3
SEM images of WSBC (a-b), nZVI (c), WSBC-nZVI nanocomposite (d-e), mapping (f-i) of WSBC-nZVI nanocomposite, surface (j), and cross-section (k, l, m) of the WSBC-nZVI membrane.

The N_2 adsorption/desorption isotherms and pore size distribution curves of the prepared nanomaterials and membrane are shown in Fig. 4. Additionally, the values related to the BET surface area and pore volume are presented in Table S1. As shown in Fig. 4, all the N_2 adsorption/desorption isotherms of the prepared nanomaterials exhibit Type IV patterns with an H_3 hysteresis loop according to the IUPAC classification, indicating the mesoporous structure of the prepared materials (Li et al., 2018). In addition, WSBC demonstrates a relatively low specific surface area (2.7 m^2/g) and pore volume (0.003 cm^3/g). However, the specific surface area and

pore volume of WSBC-nZVI displayed a significant increase (38.1 m^2/g, 0.039 cm^3/g), suggesting that nZVI with a higher specific surface area was successfully coated on the surface of WSBC. In general, the high specific surface area and porosity of nanomaterials provide more active sites for the adsorption and degradation of contaminants on the surface of the prepared materials and membrane. Similar results have been observed by Sun et al. (Sun et al., 2020). They implemented a CO_2-activated BC with a relatively high specific area for the simultaneous adsorption and degradation of phenolic pollutants in the presence of PS. Furthermore, the WSBC-nZVI membrane displayed a small average pore size of 5.13 nm, indicating that this membrane was an ultrafiltration membrane.

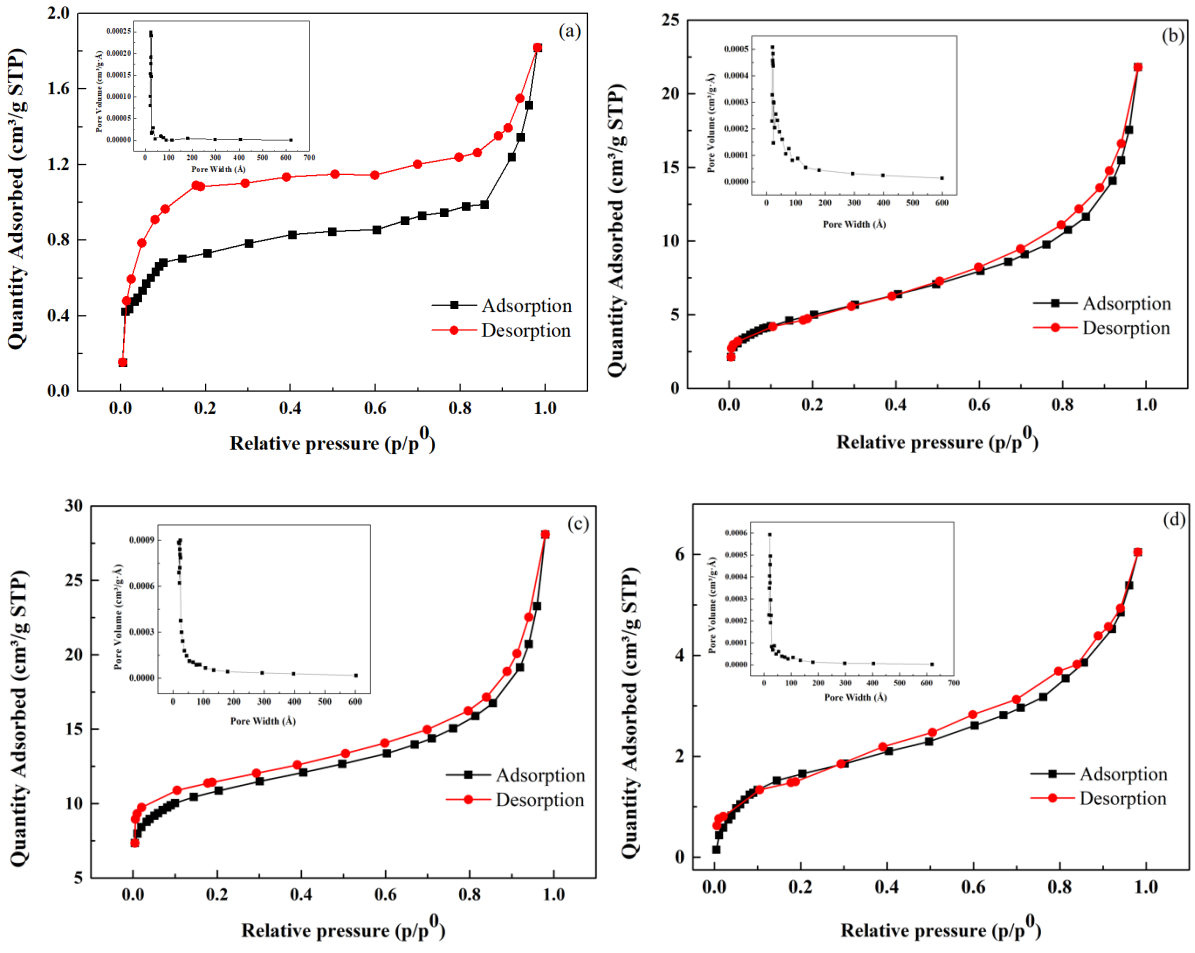

Fig. 4.

N_2 adsorption/desorption isotherms and pore size distribution curves of WSBC (a), nZVI (b), WSBC-nZVI (c), and WSBC-nZVI membrane (d).

3.2 Degradation of CBZ

The prepared nanomaterials were used for the simultaneous adsorption and degradation of CBZ as a recalcitrant pharmaceutically active compound. Fig. 5a indicates that WSBC exhibits the highest adsorption capacity for CBZ (75%) among the studied materials, which can be attributed to the presence of surface functional groups such as -COOH and -N-H on the surface of WSBC, which can provide more active sites for the adsorption of pollutants and may also promote the formation of hydrogen bonds between the adsorbent and the contaminant. This statement is supported in the recent literature. For instance, Guo et al. (Guo et al., 2021) observed that the surface functional groups (e.g., -COOH, -OH) of BC can provide more immobilization sites for Cr(III) in the adsorption process. As another example, Tran et al. (Tran et al., 2020) confirmed that the hydrogen bonds between oxygen-containing groups (e.g., -OH) of spherical biochar and paracetamol played an important role in the adsorption mechanism. In addition, both WSBC-nZVI and nZVI had low CBZ adsorption capacities (<10%). The addition of PS had no significant effect on the removal of CBZ with WSBC (Fig. 5b). In this situation, competitive adsorption occurs between CBZ and PS, and some of the adsorption sites of WSBC are occupied by PS. On the other hand, WSBC cannot efficiently activate PS to degrade CBZ. A similar phenomenon was found by Ding et al. (Ding et al., 2021). They observed that the removal efficiency of 17β-estradiol decreased from 96% to 76% by nZVI/porous graphitized BC in the presence of PS. However, as indicated in Fig. 5,b, both nZVI and WSBC-nZVI demonstrated high CBZ degradation efficiencies of 76% and 86%, respectively, indicating that these nanomaterials can efficiently activate PS for the degradation of CBZ. In addition, WSBC-nZVI exhibits a higher degradation efficiency than nZVI, which can be attributed to the high surface area, high porosity, and abundant functional groups of WSBC-nZVI. A large surface area and high porosity of nanomaterials provide more active sites for the activation of PS, resulting in more active species generated in the medium for the degradation of contaminants (Ren et al., 2021). As an example, Cai et al. (Cai et al., 2021)

demonstrated that the high surface area of manganese-doped iron-carbon composites remarkably improved the activation efficiency of PS, resulting in accelerated degradation of rhodamine B.

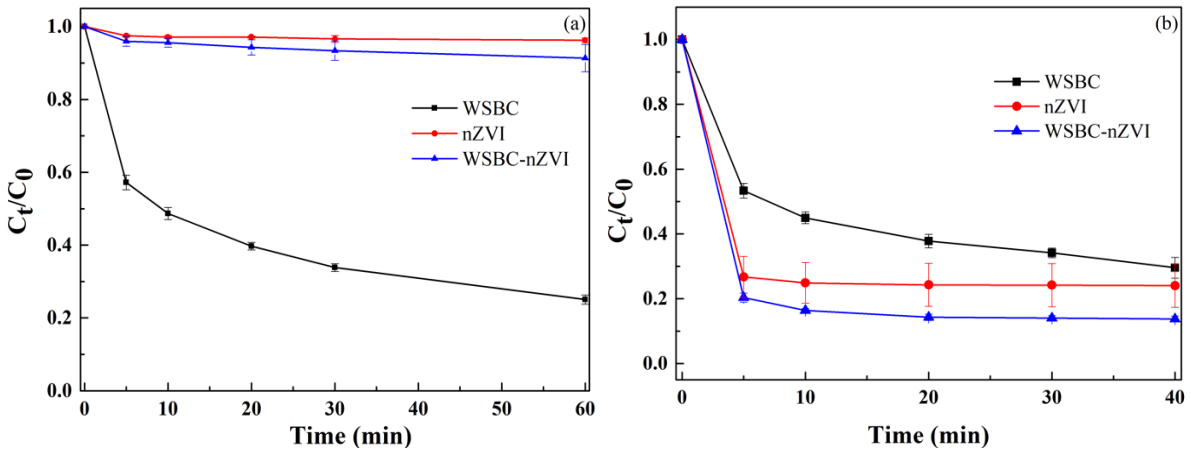

Fig. 5
Adsorption (a) and degradation (b) kinetics of CBZ by different nanomaterials (conditions: 0.5 g/L catalyst, 10 mg/L CBZ, 1 mM PS).

The effects of different parameters on CBZ degradation were also studied in the WSBC-nZVI membrane/PS system. In Fig. S1a, the removal efficiency of CBZ is only approximately 10% in the absence of PS, indicating that the membrane has a low adsorption capacity and that CBZ can pass through the membrane pores due to the relatively large pore size of the membrane. As discussed before, the pore size of the membrane is approximately 5.13 nm, and the molecular size of CBZ is less than 1 nm. Hence, this membrane cannot efficiently filter CBZ molecules. In addition, as the PS concentration increases from 0 mM to 1.5 mM, the degradation efficiency of CBZ increases from 12% to 60%, which is mainly because more PS can drive the formation of more active species, resulting in an improvement in the degradation efficiency of CBZ. Similar results have been reported previously in the literature. For instance, Yao et al. (Yao et al., 2022) demonstrated that the degradation efficiency of levofloxacin increased from 47% to 88% as the PS concentration increased from 0 mM to 4.2 mM in the $MgFe_2O_4$/biochar/PS system.

In addition, the effects of different CBZ concentrations on the degradation efficiency of the system were investigated, as indicated in Fig. S1b. The degradation efficiency of CBZ increased from 24% to 100% as the CBZ concentration decreased from 10 mg/L to 1 mg/L. This can be

because the production of active species remains constant at a certain dosage of PS. Hence, it can be concluded that under higher concentrations of CBZ, more active species are required to degrade this compound. Similar results have been reported by Bai et al. (Bai et al., 2021), who found that the degradation efficiency of bisphenol A dropped from 80% to 37% by increasing the bisphenol A concentration from 2 mg/L to 15 mg/L under a sludge-derived biochar/PS system.

The influence of the initial solution pH on the CBZ degradation efficiency is also illustrated in Fig. S1 c-d. The WSBC-nZVI membrane/PS system demonstrated a high degradation efficiency over a wide pH range (3-9), and the highest degradation efficiency was obtained at pH 6.4. CBZ has two pKa values ($pKa_1 = 2.5/pKa_2 = 13.9$) (Cortés-Arriagada et al., 2023). Hence, a weaker repulsion effect between the membrane and CBZ molecules can be expected under near-neutral pH values. Under such conditions, CBZ molecules can easily reach the surface of the membrane at pH 6.5, resulting in the efficient degradation of CBZ. Additionally, iron ions play a key role in the activation process of PS. Under acidic conditions, the release of iron ions from the membrane is accelerated by their dissolution, resulting in the deformation of the membrane surface (Shao et al., 2020). Hence, the degradation efficiency of CBZ decreased slightly at pH 3 (0.067 min^{-1}). However, the degradation efficiency dramatically decreases under alkaline conditions (pH 11). This can be due to the precipitation of iron ions in the form of less efficient iron hydroxide at high pH (Ogawa and Kawase, 2021). Under these conditions, fewer iron ions are available for the activation of PS. Furthermore, under alkaline conditions, $SO_4^{\cdot-}$ can react readily with OH^- to generate ·OH and further convert into H_2O ($SO_4^{\cdot-} + OH^- \rightarrow SO_4^{2-} + \cdot OH$) (Yan et al., 2021). Some previous papers support this hypothesis. For instance, He et al. (He et al., 2021) observed that the degradation efficiency of tetracycline decreased from 65% to 50% as the solution pH increased from 7 to 11. They also claimed that alkaline conditions are not beneficial for the activation of PS, and excess OH^- quenches $SO_4^{\cdot-}$ present in the medium.

3.3 Degradation mechanisms

The mechanisms involved in the degradation of CBZ using the WSBC-nZVI membrane/PS system were further investigated with scavenging experiments to identify the related active species such as ·OH, $SO_4^{\cdot-}$, and $^1O_2$ generated in the medium. According to previous studies, methyl alcohol (MeOH) acts as a scavenger for ·OH and $SO_4^{\cdot-}$ simultaneously, while tert-butyl-alcohol (TBA), benzoquinone (BQ), and furfuryl alcohol (FFA) are scavengers for ·OH, $O_2^{\cdot-}$ and $^1O_2$, respectively (Xue et al., 2022a). As shown in Fig. 6a-b, obvious inhibition effects were observed by the addition of TBA and especially MeOH (Fig. S2), revealing that both ·OH and $SO_4^{\cdot-}$ are generated and contribute to CBZ degradation. In addition, the degradation efficiency decreased with the addition of BQ, confirming that $O_2^{\cdot-}$ also participates in CBZ degradation. Furthermore, only 20% CBZ degradation was observed in the presence of FFA, indicating that $^1O_2$ is also produced in the degradation process. Additionally, the degradation efficiency of CBZ was the lowest with the addition of FFA among all the scavengers (Fig. S2), suggesting that $^1O_2$ plays a key role in the degradation of CBZ. Similar results have also been reported by Ma et al. (Ma et al., 2021), who confirmed that $^1O_2$ is the primary active species responsible for the degradation of reactive black 5 in the mesoporous carbon-nZVI/PS system.

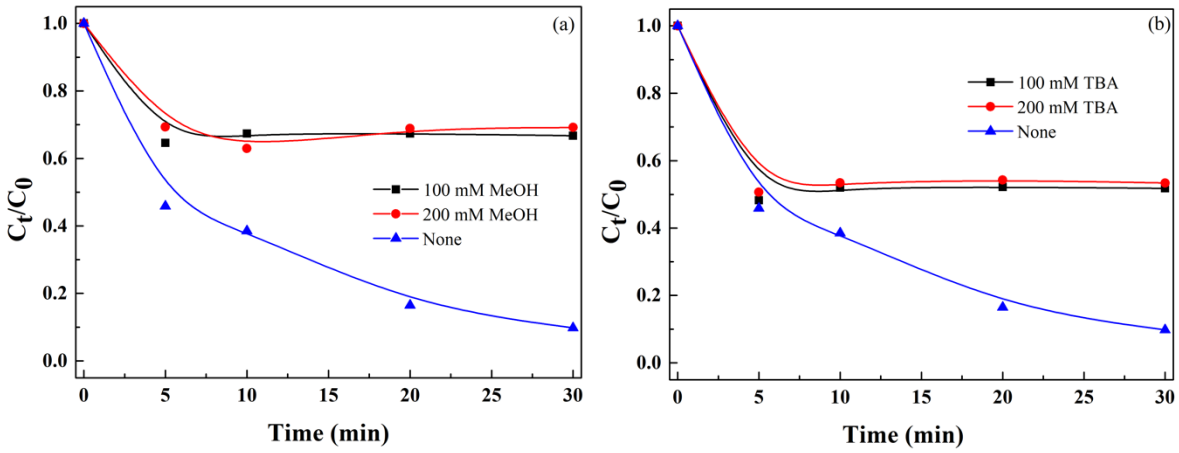

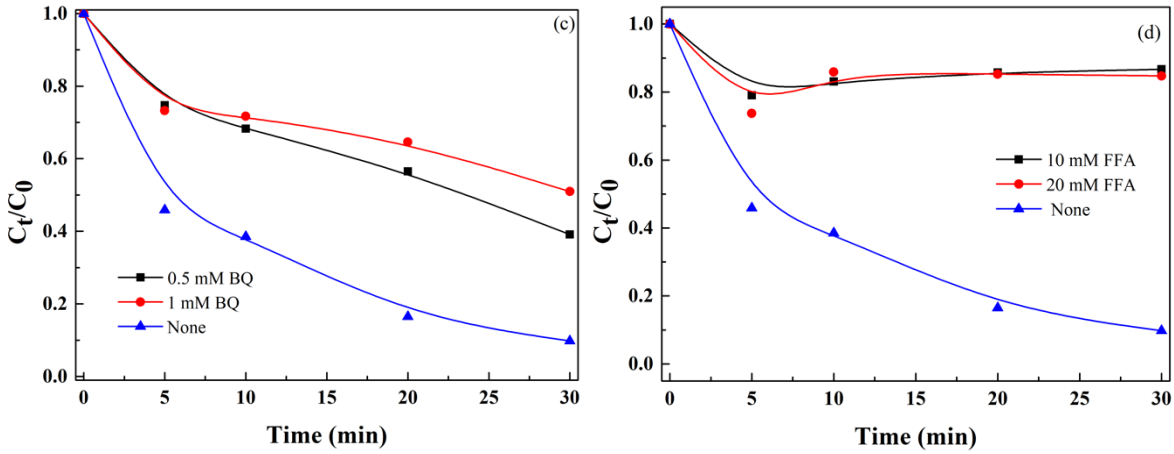

Fig. 6
The degradation efficiency of CBZ by the WSBC-nZVI membrane/PS system under different quenching conditions, MeOH (a), TBA (b), BQ (c), and FFA (d).

Fig. 7 illustrates the reaction mechanism for the WSBC-nZVI membrane/PS system proposed according to the results achieved by the scavenging experiments. The Fe species (Fe^{2+}) is quickly generated from WSBC-nZVI via different routes, such as the direct reaction of Fe^0 with PS (Equation 4), indirect reaction of Fe^0 with oxygen (Equation 5), and indirect reaction of Fe^0 with water molecules (Equation 6). (Al-Shamsi and Thomson, 2013). Subsequently, Fe^{2+} reacts with PS to produce Fe^{3+} and $SO_4^{\cdot-}$ (Equation 7). A portion of $SO_4^{\cdot-}$ is converted into SO_4^{2-} and ·OH by the reaction of H_2O or OH^- (Eq. 8-9). Diao et al. (Diao et al., 2021) also observed that ·OH can be produced based on this reaction in the BC-nZVI/peroxymonosulfate system. In addition, $O_2^{\cdot-}$ can be produced from two routes, including the reaction between Fe^{2+} and O_2 (Equation 10) and the reaction between O_2 and electrons (Equation 11). $^1O_2$ can also be generated from the reaction between $O_2^{\cdot-}$ and water (or H^+) (Equations 12-13). Meanwhile, Fe^{3+} can be reduced into Fe^{2+} through the reaction of Fe^0 and Fe^{3+} (Equation 14), which is a key reaction for the degradation of CBZ (Kim et al., 2018). In addition, WSBC as a support not only prevents the agglomeration of nZVI but also promotes the conversion of Fe^{3+} to Fe^{2+} by supplying electrons (Equation 15) (Jiang et al., 2021). Moreover, the abundant functional groups (such as -COOH and C-O) of WSBC improve the adsorption capacity for CBZ and boost the activation efficiency of PS for the degradation of organic pollutants. In conclusion, CBZ is first adsorbed on the surface of the

membrane and then decomposed in the presence of active species (e.g., ·OH, $SO4^{\cdot-}$, $O_2^{\cdot-}$, $^1O_2$). Finally, CBZ can be further oxidized into small molecular intermediates, CO_2, and H_2O (equation 16).

$$Fe^0 + S_2O_8^{2-} \rightarrow Fe^{2+} + 2SO_4^{2-} \quad (4)$$

$$2Fe^0 + O_2 + 2H_2O \rightarrow 2Fe^{2+} + 4OH^- \quad (5)$$

$$Fe^0 + 2H_2O \rightarrow Fe^{2+} + 2OH^- + H_2 \quad (6)$$

$$Fe^{2+} + S_2O_8^{2-} \rightarrow Fe^{3+} + SO_4^{\cdot-} + SO_4^{2-} \quad (7)$$

$$SO_4^{\cdot-} + H_2O \rightarrow SO_4^{2-} + H^+ + \cdot OH \quad (8)$$

$$SO_4^{\cdot-} + OH^- \rightarrow SO_4^{2-} + \cdot OH \quad (9)$$

$$Fe^{2+} + O_2 \rightarrow Fe^{3+} + O_2^{\cdot-} \quad (10)$$

$$O_2 + e^- \rightarrow O_2^{\cdot-} \quad (11)$$

$$2O_2^{\cdot-} + 2H^+ \rightarrow {}^1O_2 + H_2O_2 \quad (12)$$

$$O_2^{\cdot-} + H_2O \rightarrow {}^1O_2 + OH^- \quad (13)$$

$$Fe^0 + 2Fe^{3+} \rightarrow 3Fe^{2+} \quad (14)$$

$$Fe^{3+} + e^- \rightarrow Fe^{2+} \quad (15)$$

$$\cdot OH, SO_4^{\cdot-}, O_2^{\cdot-}, {}^1O_2 + CBZ \rightarrow \text{intermediates} \quad (16)$$

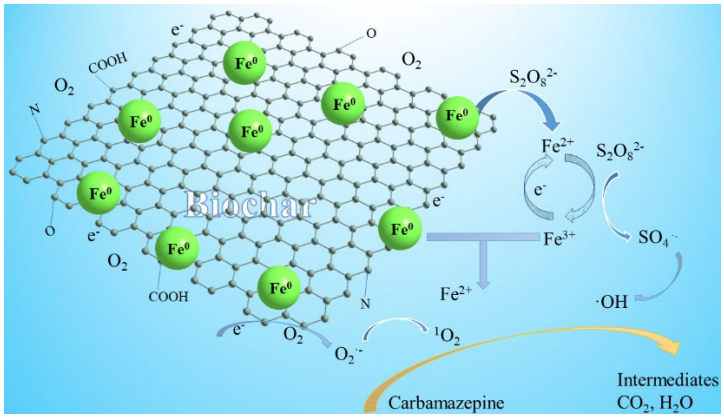

Fig. 7.
Possible reaction mechanism for the degradation of CBZ by the WSBC-nZVI membrane.

3.4 Degradation pathways of CBZ

The formation of intermediate degradation products of CBZ was explored by UPLC-MS. The detailed molecular weight values and the chemical structures of the identified intermediates are listed in Table S2. Fig. 8 demonstrates the possible degradation pathways. According to pathway I, the aliphatic double bond was attacked by the active species to obtain P1, which was further hydroxylated to generate intermediate P5. P1 was also converted into P2 by a deamination step. In pathway II, P4 was produced by the hydration of CBZ, which was further transformed into a heterocyclic radical to obtain P5. Then, P6 was obtained from P5 by the formation of a heterocycle. Lai et al. (Lai et al., 2021) observed similar degradation pathways of CBZ based on the identified intermediates and a Fukui function calculation in the V-Fe concentrate ore/PS system. In pathway III, P7 was produced by the oxidation of CBZ, and then P8 was obtained from P7 through a further aldehyde oxidation process. Moreover, P8 was transformed into P6 by closed-loop and dehydration reactions. Subsequently, P3 was produced from P6 by losing an amidogen group. P10 was generated through the deketonization of P3, and then P11 was obtained by further oxidation of P10. In addition, P6 could be oxidized to the produced carboxylic acid product of P9. Then, P11 was also obtained from P9 by losing the acrylamide and carboxylic acid groups. Finally, P10 and P11 were converted into small molecules of P12 and P13 through ring cleavage reactions. A similar ring cleavage degradation pathway of CBZ was found for the $Bi_2S_3/BiVO_4/MgIn_2S_4$/visible light system (Guo et al., 2019).

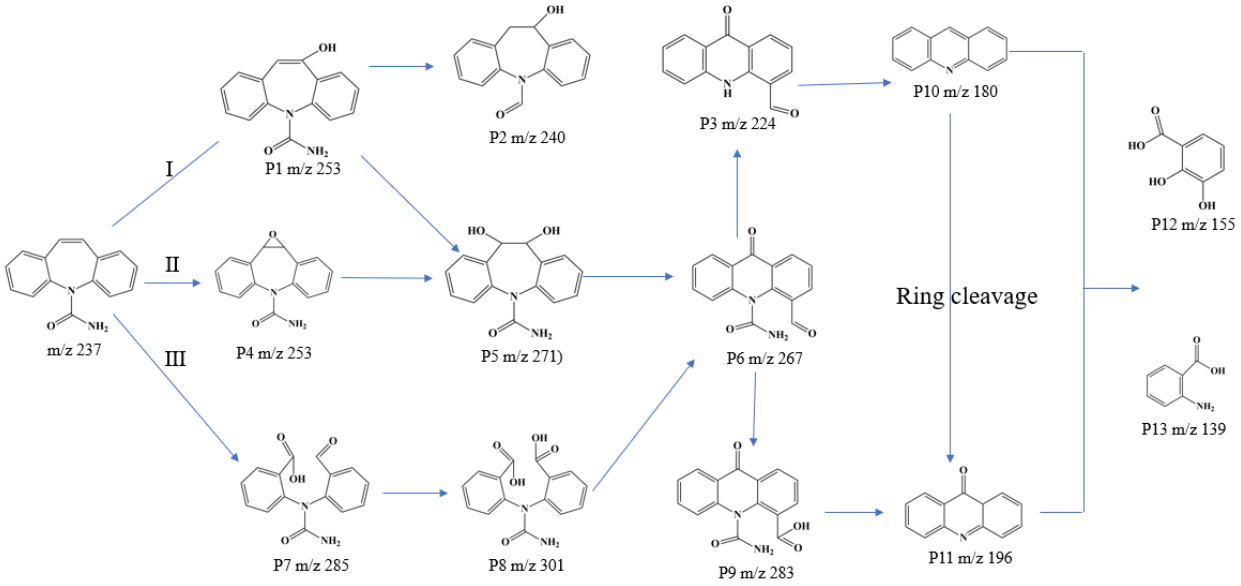

435

436

437 **Fig. 8.**
438 Proposed degradation pathways of CBZ in the membrane/PS system.

439 The toxicity of CBZ and its intermediates in the degradation process was estimated by ECOSAR
440 modelling. According to the Globally Harmonized System of Classification and Labelling of
441 Chemicals, the results can be classified as very toxic, toxic, harmful, and not harmful (Xu et al.,
442 2021), as shown in Tables S3 and S4. The half lethal concentration (LC50) values of CBZ for fish
443 and daphnids and the half effective concentration (EC50) values for green algae were 40.9 mg/L,
444 14.1 mg/L, and 0.260 mg/L, respectively. Additionally, the chronic toxicity value (ChV) values of
445 CBZ for fish, daphnid, and green algae were 1.05 mg/L, 1.17 mg/L, and 0.096 mg/L, respectively.
446 These results confirmed that CBZ has high acute and chronic toxicity for aquatic organisms.
447 Fortunately, most of the degradation products of CBZ have lower toxicity than CBZ (Fig. 9),
448 revealing that most of the CBZ has been converted into low toxicity products in the degradation
449 process. However, P4 is at a very toxic level for fish (chronic toxicity), suggesting that the
450 degradation products also need to be given more attention. Overall, the WSBC-nZVI
451 membrane/PS system can be considered an efficient technology for the treatment of CBZ-
452 containing wastewater.

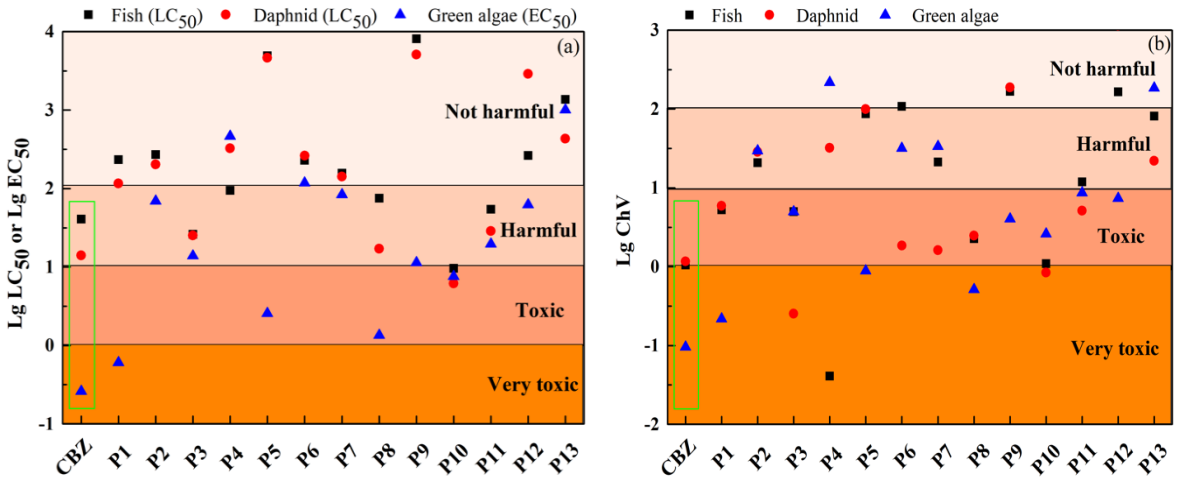

Fig. 9
Predicted acute (a) and chronic toxicity values (b) of CBZ and its intermediates based on ECOSAR estimation.

3.5 Degradation of CBZ in real wastewater

To investigate the practical viability of the WSBC-nZVI membrane/PS system in real wastewater treatment, a secondary effluent from a local municipal wastewater treatment plant (Aquafin, Mechelen-Noord, Belgium) was used to test the removal efficiency of CBZ. According to Fig. 10a, the membrane exhibits a high water permeability of 108 L/(m²·h·bar) in Milli-Q water. This can be attributed to a low mass transfer resistance by the high porosity and surface hydrophilic oxygen-containing groups of the membrane, resulting in water easily passing through the membrane. In addition, WSBC-nZVI in the membrane provides channels for water transport and improves the waster permeability of the membrane. Similar results were reported by Zhang et al. (Zhang et al., 2021). They observed that the biochar-polydopamine membrane had a higher water permeability of 32 L/(m²·h·bar) than the polydopamine membrane (18 L/(m²·h·bar)). However, the water permeability of the membrane dramatically decreases to 63 L/(m²·h·bar) in real wastewater. This is attributed to pore blocking by the suspended solids in real wastewater, resulting in an increase in mass transfer resistance for water to pass through the membrane. In addition, the water permeability was similar with (63.7 L/(m²·h·bar)) and without PS (62.5 L/(m²·h·bar)), mainly because the active species from the activation process of PS are not efficient for the decomposition of suspended solids; hence, the mass transfer resistance of

water is similar under such conditions. As illustrated in Fig. 10b, the initial COD value of real wastewater (50 mg/L) decreases to 40 mg/L after a separation process, which can be related to the suspended solids being rejected by the membrane due to the large size of suspended solids. In the presence of PS, the COD removal efficiency was similar to that of the separation process, suggesting that the active species cannot efficiently decompose suspended solids and organic pollutants, which is consistent with the water permeability results. This is mainly because the active species are insufficient for the degradation of all the compounds. Moreover, as illustrated in Fig. 10c, the WSBC-nZVI membrane/PS system exhibits a high degradation efficiency of 90% for CBZ in Milli-Q water. However, this system presents a low degradation efficiency for real wastewater, which can be attributed to the fact that the composition is quite complex in real wastewater due to the presence of suspended solids, inorganic ions, organic pollutants, etc. Hence, efficient treatment of such an effluent requires more active species generated in the medium. Reports available in the literature also support this statement. For instance, Rajabi et al. (Rajabi et al., 2022) demonstrated that the degradation efficiency of metronidazole decreased from 100% to 45% in real wastewater in a $CuCoFe_2O_4$@methylcellulose activated carbon/PS system. They speculated that the decomposition of impurities in real wastewater requires more active species, and some cations and anions act as scavengers for the generated oxidative species, which reduces the number of free radicals available in this system. The application of combined methods (e.g., sedimentation, separation, biodegradation, AOPs) with membrane separation can also be considered for the efficient treatment of real wastewater.

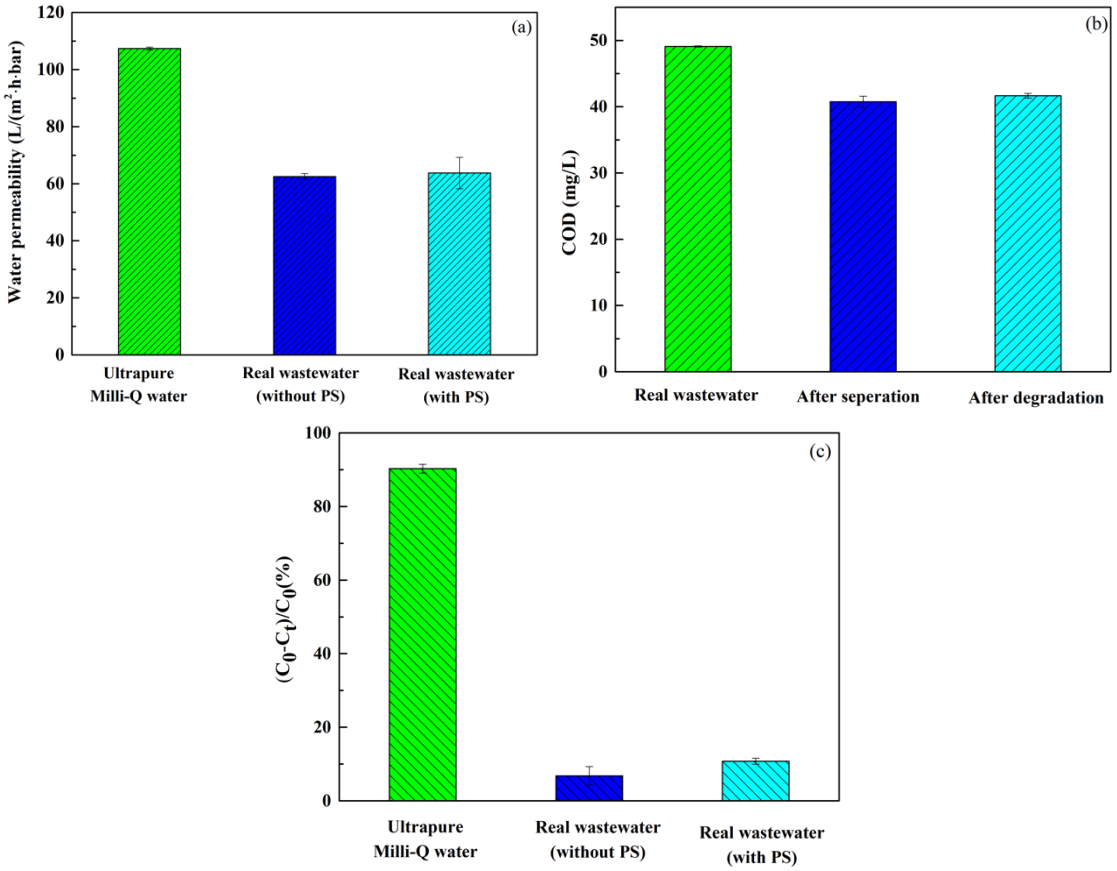

Fig. 10.
Water permeability (CBZ, PS) of the membrane (a), COD values of the wastewater (b), and the degradation efficiency of CBZ in real wastewater (initial pH, 1 mM PMS, 2 mg/L CBZ).

3.6 Stability of the membrane

The stability of the membrane was studied by reuse experiments and FTIR characterization. The membrane was used three times without any cleaning procedure. As shown in Fig. S3a, the degradation efficiency of CBZ remained at approximately 90% after three runs, but the degradation reaction rate constant of CBZ decreased slightly from 0.08 min^{-1} to 0.06 min^{-1}. This can be attributed to the fact that some of the active sites in the membrane are occupied by the degradation intermediates of the previous runs, preventing the formation of sufficient active species for CBZ degradation. Nevertheless, the degradation efficiency of CBZ was still acceptable after three reuse experiments. In addition, the water permeability of the membrane remained quasi stable after three reuse experiments (108 L/(m^2·h·bar), 96 L/(m^2·h·bar), 101 L/(m^2·h·bar)) (Fig. S3b), revealing that the pores of the membrane structure with an average pore size

distribution of 5.13 nm are not blocked by CBZ and its degradation products due to the small size of CBZ (less than 1 nm) and large pore size of the membrane. Moreover, the FTIR spectra (Fig. S3c) of the fresh membrane and the spent membrane are similar, suggesting no serious deformation in the membrane structure because of the formation of active species generated in the medium. In conclusion, the prepared WSBC-nZVI membrane is very stable.

4. Conclusions

In this research, walnut shell biochar (WSBC), nano zero-valent iron (nZVI), and walnut shell biochar-nano zero-valent iron (WSBC-nZVI) were synthesized for the degradation of carbamazepine (CBZ) in the presence of persulfate (PS). WSBC-nZVI displayed the highest removal efficiency of 86% for CBZ among the prepared nanomaterials (70% for WSBC, 76% for nZVI, 0.5 g/L catalyst, 10 mg/L CBZ, 1 mM persulfate). When applying the WBC-nZVI membrane in a dead-end configuration, the results showed that for a CBZ concentration of 2 mg/L and a persulfate concentration of 1 mM, 91% of the compound was removed within 30 min of reaction. The degradation mechanisms were discussed based on scavenging experiments, and the results indicated that the formation of singlet oxygen is the dominant mechanism for the degradation of CBZ in this system. The degradation products were also identified by using ultrahigh-performance liquid chromatography in combination with high-resolution mass spectrometry (UHPLC-QTOF-MS), and their potential ecotoxicological effects were evaluated using the ECOSAR database. The results demonstrated that most of the intermediates are of a lower toxicity level than CBZ. The feasibility of the membrane/PS system was also investigated by the treatment of real wastewater. Moreover, reuse experiments confirmed that the membrane is stable and efficient for the degradation of organic compounds.

Acknowledgements

Yongtao Xue would like to acknowledge the China Scholarship Council (CSC) of the Ministry of Education, P. R. China (CSC NO. 202009505003).

Reference

Ahmad, S.Z.N., Salleh, W.N.W., Ismail, A.F., Yusof, N., Yusop, M.Z.M., Aziz, F., 2020. Adsorptive removal of heavy metal ions using graphene-based nanomaterials: Toxicity, roles of functional groups and mechanisms. Chemosphere 248, 126008.

Al-Shamsi, M.A., Thomson, N.R., 2013. Treatment of Organic Compounds by Activated Persulfate Using Nanoscale Zerovalent Iron. Ind Eng Chem Res 52, 13564–13571. https://doi.org/10.1021/ie400387p

Bai, X., Zhang, Y., Shi, J., Xu, L., Wang, Y., Jin, P., 2021. A new application pattern for sludge-derived biochar adsorbent: Ideal persulfate activator for the high-efficiency mineralization of pollutants. J Hazard Mater 419, 126343. https://doi.org/https://doi.org/10.1016/j.jhazmat.2021.126343

Boguta, P., Sokołowska, Z., Skic, K., Tomczyk, A., 2019. Chemically engineered biochar – Effect of concentration and type of modifier on sorption and structural properties of biochar from wood waste. Fuel 256, 115893. https://doi.org/https://doi.org/10.1016/j.fuel.2019.115893

Cai, M., Zhang, Y., Dong, C., Wu, W., Wang, Q., Song, Z., Shi, Y., Wu, L., Jin, M., Dionysiou, D.D., Wei, Z., 2021. Manganese doped iron–carbon composite for synergistic persulfate activation: Reactivity, stability, and mechanism. J Hazard Mater 405, 124228. https://doi.org/https://doi.org/10.1016/j.jhazmat.2020.124228

Chen, K., Ma, D., Yu, H., Zhang, S., Seyler, B.C., Chai, Z., Peng, S., 2022. Biosorption of V(V) onto Lantana camara biochar modified by H3PO4: Characteristics, mechanism, and regenerative capacity. Chemosphere 291, 132721. https://doi.org/https://doi.org/10.1016/j.chemosphere.2021.132721

Chen, Y., Ho, S.-H., Wang, D., Wei, Z., Chang, J.-S., Ren, N., 2018. Lead removal by a magnetic biochar derived from persulfate-ZVI treated sludge together with one-pot pyrolysis. Bioresour Technol 247, 463–470. https://doi.org/https://doi.org/10.1016/j.biortech.2017.09.125

Cortés-Arriagada, D., Miranda-Rojas, S., Camarada, M.B., Ortega, D.E., Alarcón-Palacio, V.B., 2023. The interaction mechanism of polystyrene microplastics with pharmaceuticals and personal care products. Science of The Total Environment 861, 160632. https://doi.org/https://doi.org/10.1016/j.scitotenv.2022.160632

Diao, Z.-H., Zhang, W.-X., Liang, J.-Y., Huang, S.-T., Dong, F.-X., Yan, L., Qian, W., Chu, W., 2021. Removal of herbicide atrazine by a novel biochar based iron composite coupling with peroxymonosulfate process from soil: Synergistic effect and mechanism. Chemical Engineering Journal 409, 127684. https://doi.org/https://doi.org/10.1016/j.cej.2020.127684

Dilshad, M.R., Islam, A., Hamidullah, U., Jamshaid, F., Ahmad, A., Butt, M.T.Z., Ijaz, A., 2019. Effect of alumina on the performance and characterization of cross-linked PVA/PEG 600 blended membranes for CO2/N2 separation. Sep Purif Technol 210, 627–635. https://doi.org/https://doi.org/10.1016/j.seppur.2018.08.026

Ding, J., Xu, W., Liu, S., Liu, Y., Tan, X., Li, X., Li, Z., Zhang, P., Du, L., Li, M., 2021. Activation of persulfate by nanoscale zero-valent iron loaded porous graphitized biochar for the

removal of 17β-estradiol: Synthesis, performance and mechanism. J Colloid Interface Sci 588, 776–786. https://doi.org/https://doi.org/10.1016/j.jcis.2020.11.111

Fan, M., Zhang, P., Wang, C., Tang, J., Sun, H., 2022. Tailored design of three-dimensional rGOA-nZVI catalyst as an activator of persulfate for degradation of organophosphorus pesticides. J Hazard Mater 428, 128254. https://doi.org/https://doi.org/10.1016/j.jhazmat.2022.128254

Fan, Y., Zhou, Y., Feng, Y., Wang, P., Li, X., Shih, K., 2020. Fabrication of reactive flat-sheet ceramic membranes for oxidative degradation of ofloxacin by peroxymonosulfate. J Memb Sci 611, 118302. https://doi.org/https://doi.org/10.1016/j.memsci.2020.118302

Gu, H., Gao, Y., Xiong, M., Zhang, D., Chen, W., Xu, Z., 2021. Removal of nitrobenzene from aqueous solution by graphene/biochar supported nanoscale zero-valent-iron: Reduction enhancement behavior and mechanism. Sep Purif Technol 275, 119146. https://doi.org/https://doi.org/10.1016/j.seppur.2021.119146

Guo, N., Lv, X., Yang, Q., Xu, X., Song, H., 2021. Effective removal of hexavalent chromium from aqueous solution by ZnCl2 modified biochar: Effects and response sequence of the functional groups. J Mol Liq 334, 116149. https://doi.org/https://doi.org/10.1016/j.molliq.2021.116149

Guo, Y., Ao, Y., Wang, P., Wang, C., 2019. Mediator-free direct dual-Z-scheme Bi2S3/BiVO4/MgIn2S4 composite photocatalysts with enhanced visible-light-driven performance towards carbamazepine degradation. Appl Catal B 254, 479–490. https://doi.org/https://doi.org/10.1016/j.apcatb.2019.04.031

Han, L., Xue, S., Zhao, S., Yan, J., Qian, L., Chen, M., 2015. Biochar Supported Nanoscale Iron Particles for the Efficient Removal of Methyl Orange Dye in Aqueous Solutions. PLoS One 10, e0132067–e0132067. https://doi.org/10.1371/journal.pone.0132067

He, J., Song, Y., Chen, J.P., 2017. Development of a novel biochar/PSF mixed matrix membrane and study of key parameters in treatment of copper and lead contaminated water. Chemosphere 186, 1033–1045. https://doi.org/https://doi.org/10.1016/j.chemosphere.2017.07.028

He, J., Tang, J., Zhang, Z., Wang, L., Liu, Q., Liu, X., 2021. Magnetic ball-milled FeS@biochar as persulfate activator for degradation of tetracycline. Chemical Engineering Journal 404, 126997. https://doi.org/https://doi.org/10.1016/j.cej.2020.126997

Heng, Z.W., Chong, W.C., Pang, Y.L., Sim, L.C., Koo, C.H., 2021. Novel visible-light responsive NCQDs-TiO2/PAA/PES photocatalytic membrane with enhanced antifouling properties and self-cleaning performance. J Environ Chem Eng 9, 105388. https://doi.org/https://doi.org/10.1016/j.jece.2021.105388

Jiang, Q., Zhang, Y., Jiang, S., Wang, Y., Li, H., Han, W., Qu, J., Wang, L., Hu, Y., 2021. Graphene-like carbon sheet-supported nZVI for efficient atrazine oxidation degradation by persulfate activation. Chemical Engineering Journal 403, 126309. https://doi.org/https://doi.org/10.1016/j.cej.2020.126309

614 Kim, C., Ahn, J.-Y., Kim, T.Y., Shin, W.S., Hwang, I., 2018. Activation of Persulfate by Nanosized
615 Zero-Valent Iron (NZVI): Mechanisms and Transformation Products of NZVI. Environ Sci
616 Technol 52, 3625–3633. https://doi.org/10.1021/acs.est.7b05847

617 Lai, L., Ji, H., Zhang, H., Liu, R., Zhou, C., Liu, W., Ao, Z., Li, N., Liu, C., Yao, G., Lai, B., 2021.
618 Activation of peroxydisulfate by V-Fe concentrate ore for enhanced degradation of
619 carbamazepine: Surface ≡V(III) and ≡V(IV) as electron donors promoted the regeneration
620 of ≡Fe(II). Appl Catal B 282, 119559.
621 https://doi.org/https://doi.org/10.1016/j.apcatb.2020.119559

622 Li, C., Zhang, L., Gao, Y., Li, A., 2018. Facile synthesis of nano ZnO/ZnS modified biochar by
623 directly pyrolyzing of zinc contaminated corn stover for Pb(II), Cu(II) and Cr(VI) removals.
624 Waste Management 79, 625–637.
625 https://doi.org/https://doi.org/10.1016/j.wasman.2018.08.035

626 Li, F., Li, L., Zhong, G., Zhai, Y., Li, Z., 2019. Effects of ultrasonic time, size of aggregates and
627 temperature on the stability and viscosity of Cu-ethylene glycol (EG) nanofluids. Int J Heat
628 Mass Transf 129, 278–286.
629 https://doi.org/https://doi.org/10.1016/j.ijheatmasstransfer.2018.09.104

630 Li, J., Lin, Q., Luo, H., Fu, H., Wu, L., Chen, Y., Ma, Y., 2022. The effect of nanoscale zero-valent
631 iron-loaded N-doped biochar on the generation of free radicals and nonradicals by
632 peroxydisulfate activation. Journal of Water Process Engineering 47, 102681.
633 https://doi.org/https://doi.org/10.1016/j.jwpe.2022.102681

634 Li, S., Tang, J., Liu, Q., Liu, X., Gao, B., 2020. A novel stabilized carbon-coated nZVI as
635 heterogeneous persulfate catalyst for enhanced degradation of 4-chlorophenol. Environ Int
636 138, 105639. https://doi.org/https://doi.org/10.1016/j.envint.2020.105639

637 Li, W., Cheng, C., He, L., Liu, M., Cao, G., Yang, S., Ren, N., 2021. Effects of feedstock and
638 pyrolysis temperature of biochar on promoting hydrogen production of ethanol-type
639 fermentation. Science of The Total Environment 790, 148206.
640 https://doi.org/https://doi.org/10.1016/j.scitotenv.2021.148206

641 Liu, S., Zhou, A., Fan, Y., Duan, Y., Liu, Z., He, Z., Liu, W., Yue, X., 2023. Using heat-activated
642 persulfate to accelerate short-chain fatty acids production from waste activated sludge
643 fermentation triggered by sulfate-reducing microbial consortium. Science of The Total
644 Environment 861, 160795.
645 https://doi.org/https://doi.org/10.1016/j.scitotenv.2022.160795

646 Liu, Y., Guo, R., Shen, G., Li, Yunhe, Li, Yuanqing, Gou, J., Cheng, X., 2021. Construction of
647 CuO@CuS/PVDF composite membrane and its superiority for degradation of antibiotics by
648 activation of persulfate. Chemical Engineering Journal 405, 126990.
649 https://doi.org/https://doi.org/10.1016/j.cej.2020.126990

650 Luo, X., Liang, H., Qu, F., Ding, A., Cheng, X., Tang, C.Y., Li, G., 2018. Free-standing
651 hierarchical α-MnO2@CuO membrane for catalytic filtration degradation of organic
652 pollutants. Chemosphere 200, 237–247.
653 https://doi.org/https://doi.org/10.1016/j.chemosphere.2018.02.113

Ma, Z., Cao, H., Lv, F., Yang, Y., Chen, C., Yang, T., Zheng, H., Wu, D., 2021. Preparation of nZVI embedded modified mesoporous carbon for catalytic persulfate to degradation of reactive black 5. Front Environ Sci Eng 15, 98. https://doi.org/10.1007/s11783-020-1372-4

Mandal, S., Pu, S., Shangguan, L., Liu, S., Ma, H., Adhikari, S., Hou, D., 2020. Synergistic construction of green tea biochar supported nZVI for immobilization of lead in soil: A mechanistic investigation. Environ Int 135, 105374. https://doi.org/https://doi.org/10.1016/j.envint.2019.105374

Monteagudo, J.M., El-taliawy, H., Durán, A., Caro, G., Bester, K., 2018. Sono-activated persulfate oxidation of diclofenac: Degradation, kinetics, pathway and contribution of the different radicals involved. J Hazard Mater 357, 457–465. https://doi.org/https://doi.org/10.1016/j.jhazmat.2018.06.031

Ogawa, T., Kawase, Y., 2021. Effect of solution pH on removal of anionic surfactant sodium dodecylbenzenesulfonate (SDBS) from model wastewater using nanoscale zero-valent iron (nZVI). J Environ Chem Eng 9, 105928. https://doi.org/https://doi.org/10.1016/j.jece.2021.105928

Qi, C., Liu, X., Lin, C., Zhang, X., Ma, J., Tan, H., Ye, W., 2014. Degradation of sulfamethoxazole by microwave-activated persulfate: Kinetics, mechanism and acute toxicity. Chemical Engineering Journal 249, 6–14. https://doi.org/https://doi.org/10.1016/j.cej.2014.03.086

Rajabi, S., Nasiri, A., Hashemi, M., 2022. Enhanced activation of persulfate by CuCoFe2O4@MC/AC as a novel nanomagnetic heterogeneous catalyst with ultrasonic for metronidazole degradation. Chemosphere 286, 131872. https://doi.org/https://doi.org/10.1016/j.chemosphere.2021.131872

Ren, X., Wang, Jingjing, Yu, J., Song, B., Feng, H., Shen, M., Zhang, H., Zou, J., Zeng, G., Tang, L., Wang, Jiajia, 2021. Waste valorization: Transforming the fishbone biowaste into biochar as an efficient persulfate catalyst for degradation of organic pollutant. J Clean Prod 291, 125225. https://doi.org/https://doi.org/10.1016/j.jclepro.2020.125225

Roy, K., Moholkar, V.S., 2021. Mechanistic analysis of carbamazepine degradation in hybrid advanced oxidation process of hydrodynamic cavitation/UV/persulfate in the presence of ZnO/ZnFe2O4. Sep Purif Technol 270, 118764. https://doi.org/https://doi.org/10.1016/j.seppur.2021.118764

Shan, A., Idrees, A., Zaman, W.Q., Abbas, Z., Ali, M., Rehman, M.S.U., Hussain, S., Danish, M., Gu, X., Lyu, S., 2021. Synthesis of nZVI-Ni@BC composite as a stable catalyst to activate persulfate: Trichloroethylene degradation and insight mechanism. J Environ Chem Eng 9, 104808. https://doi.org/https://doi.org/10.1016/j.jece.2020.104808

Shao, S., Qian, L., Zhan, X., Wang, M., Lu, K., Peng, J., Miao, D., Gao, S., 2020. Transformation and toxicity evolution of amlodipine mediated by cobalt ferrite activated peroxymonosulfate: Effect of oxidant concentration. Chemical Engineering Journal 382, 123005. https://doi.org/https://doi.org/10.1016/j.cej.2019.123005

Silvestri, D., Wacławek, S., Sobel, B., Torres–Mendieta, R., Pawlyta, M., Padil, V.V.T., Filip, J., Černík, M., 2021. Modification of nZVI with a bio-conjugate containing amine and carbonyl functional groups for catalytic activation of persulfate. Sep Purif Technol 257, 117880. https://doi.org/https://doi.org/10.1016/j.seppur.2020.117880

696 Soria, R.I., Rolfe, S.A., Betancourth, M.P., Thornton, S.F., 2020. The relationship between
697 properties of plant-based biochars and sorption of Cd(II), Pb(II) and Zn(II) in soil model
698 systems. Heliyon 6, e05388.
699 https://doi.org/https://doi.org/10.1016/j.heliyon.2020.e05388

700 Su, H., Dou, X., Xu, D., Feng, L., Liu, Y., Du, Z., Zhang, L., 2022. Fe0-loaded superfine
701 powdered activated carbon prepared by ball milling for synergistic adsorption and
702 persulfate activation to remove aqueous carbamazepine. Chemosphere 293, 133665.
703 https://doi.org/https://doi.org/10.1016/j.chemosphere.2022.133665

704 Sun, C., Chen, T., Huang, Q., Zhan, M., Li, X., Yan, J., 2020. Activation of persulfate by CO2-
705 activated biochar for improved phenolic pollutant degradation: Performance and
706 mechanism. Chemical Engineering Journal 380, 122519.
707 https://doi.org/https://doi.org/10.1016/j.cej.2019.122519

708 Tang, J., Zhang, C., Shi, X., Sun, J., Cunningham, J.A., 2019. Municipal wastewater treatment
709 plants coupled with electrochemical, biological and bio-electrochemical technologies:
710 Opportunities and challenge toward energy self-sufficiency. J Environ Manage 234, 396–
711 403. https://doi.org/https://doi.org/10.1016/j.jenvman.2018.12.097

712 Tran, H.N., Tomul, F., Thi Hoang Ha, N., Nguyen, D.T., Lima, E.C., Le, G.T., Chang, C.T.,
713 Masindi, V., Woo, S.H., 2020. Innovative spherical biochar for pharmaceutical removal
714 from water: Insight into adsorption mechanism. J Hazard Mater 394, 122255.
715 https://doi.org/10.1016/j.jhazmat.2020.122255

716 Wang, B., Deng, C., Ma, W., Sun, Y., 2021. Modified nanoscale zero-valent iron in persulfate
717 activation for organic pollution remediation: a review. Environmental Science and
718 Pollution Research 28, 34229–34247. https://doi.org/10.1007/s11356-021-13972-w

719 Wen, M., Li, G., Liu, H., Chen, J., An, T., Yamashita, H., 2019. Metal–organic framework-based
720 nanomaterials for adsorption and photocatalytic degradation of gaseous pollutants: recent
721 progress and challenges. Environ Sci Nano 6, 1006–1025.

722 Wu, G., Kong, W., Gao, Y., Kong, Y., Dai, Z., Dan, H., Shang, Y., Wang, S., Yin, F., Yue, Q., Gao,
723 B., 2022. Removal of chloramphenicol by sulfide-modified nanoscale zero-valent iron
724 activated persulfate: Performance, salt resistance, and reaction mechanisms. Chemosphere
725 286, 131876. https://doi.org/https://doi.org/10.1016/j.chemosphere.2021.131876

726 Xiao, S., Cheng, M., Zhong, H., Liu, Z., Liu, Y., Yang, X., Liang, Q., 2020. Iron-mediated
727 activation of persulfate and peroxymonosulfate in both homogeneous and heterogeneous
728 ways: A review. Chemical Engineering Journal 384, 123265.
729 https://doi.org/10.1016/j.cej.2019.123265

730 Xu, J., Zhang, X., Sun, C., He, H., Dai, Y., Yang, S., Lin, Y., Zhan, X., Li, Q., Zhou, Y., 2018.
731 Catalytic Degradation of Diatrizoate by Persulfate Activation with Peanut Shell Biochar-
732 Supported Nano Zero-Valent Iron in Aqueous Solution. International Journal of
733 Environmental Research and Public Health . https://doi.org/10.3390/ijerph15091937

734 Xu, M., Deng, J., Cai, A., Ye, C., Ma, X., Li, Q., Zhou, S., Li, X., 2021. Synergistic effects of UVC
735 and oxidants (PS vs. Chlorine) on carbamazepine attenuation: Mechanism, pathways, DBPs
736 yield and toxicity assessment. Chemical Engineering Journal 413, 127533.
737 https://doi.org/https://doi.org/10.1016/j.cej.2020.127533

738 Xue, Y., Guo, Y., Zhang, X., Kamali, M., M. Aminabhavi, T., Appels, L., Dewil, R., 2022a.
739 Efficient adsorptive removal of ciprofloxacin and carbamazepine using modified pinewood
740 biochar – A kinetic, mechanistic study. Chemical Engineering Journal 450, 137896.
741 https://doi.org/https://doi.org/10.1016/j.cej.2022.137896

742 Xue, Y., Kamali, M., Yu, X., Appels, L., Dewil, R., 2022b. Novel CuO/Cu2(V2O7)/V2O5
743 composite membrane as an efficient catalyst for the activation of persulfate toward
744 ciprofloxacin degradation. Chemical Engineering Journal 140201.
745 https://doi.org/https://doi.org/10.1016/j.cej.2022.140201

746 Xue, Y., Kamali, M., Zhang, X., Askari, N., De Preter, C., Appels, L., Dewil, R., 2023.
747 Immobilization of photocatalytic materials for (waste)water treatment using 3D printing
748 technology – advances and challenges. Environmental Pollution 316, 120549.
749 https://doi.org/https://doi.org/10.1016/j.envpol.2022.120549

750 Yan, Z., Gu, Y., Wang, X., Hu, Y., Li, X., 2021. Degradation of aniline by ferrous ions activated
751 persulfate: Impacts, mechanisms, and by-products. Chemosphere 268, 129237.
752 https://doi.org/https://doi.org/10.1016/j.chemosphere.2020.129237

753 Yang, Y., Luo, J., Ding, Y., Song, P., Xia, L., 2022. Porous Au/γ-AlOOH Nanoflowers for Surface-
754 Enhanced Raman Scattering Detection of Aromatic Acid Compounds. ACS Appl Nano
755 Mater 5, 852–861. https://doi.org/10.1021/acsanm.1c03566

756 Yao, B., Luo, Z., Du, S., Yang, J., Zhi, D., Zhou, Y., 2022. Magnetic MgFe2O4/biochar derived
757 from pomelo peel as a persulfate activator for levofloxacin degradation: Effects and
758 mechanistic consideration. Bioresour Technol 346, 126547.
759 https://doi.org/https://doi.org/10.1016/j.biortech.2021.126547

760 Yu, Y., Chen, D., Xie, S., Sun, Q., Zhang, Z.-X., Zeng, G., 2022. Adsorption behavior of
761 carbamazepine on Zn-MOFs derived nanoporous carbons: Defect enhancement, role of N
762 doping and adsorption mechanism. J Environ Chem Eng 10, 107660.
763 https://doi.org/https://doi.org/10.1016/j.jece.2022.107660

764 Zhang, D., Zhang, K., Hu, X., Xue, Y., Zhang, L., Sun, Y., 2021. Ball-milled biochar incorporated
765 polydopamine thin-film composite (PDA/TFC) membrane for high-flux separation of
766 tetracyclic antibiotics from wastewater. Sep Purif Technol 272, 118957.
767 https://doi.org/https://doi.org/10.1016/j.seppur.2021.118957

768 Zheng, J., Li, Y., Xu, D., Zhao, R., Liu, Y., Li, G., Gao, Q., Zhang, X., Volodine, A., Van der
769 Bruggen, B., 2022. Facile fabrication of a positively charged nanofiltration membrane for
770 heavy metal and dye removal. Sep Purif Technol 282, 120155.
771 https://doi.org/https://doi.org/10.1016/j.seppur.2021.120155

772 Zhou, H., Lai, L., Wan, Y., He, Y., Yao, G., Lai, B., 2020. Molybdenum disulfide (MoS2): A
773 versatile activator of both peroxymonosulfate and persulfate for the degradation of
774 carbamazepine. Chemical Engineering Journal 384, 123264.
775 https://doi.org/https://doi.org/10.1016/j.cej.2019.123264

776 Zhou, X., Zeng, Z., Zeng, G., Lai, C., Xiao, R., Liu, S., Huang, D., Qin, L., Liu, X., Li, B., Yi, H.,
777 Fu, Y., Li, L., Zhang, M., Wang, Z., 2020. Insight into the mechanism of persulfate activated
778 by bone char: Unraveling the role of functional structure of biochar. Chemical Engineering
779 Journal 401, 126127. https://doi.org/https://doi.org/10.1016/j.cej.2020.126127

780 Zybina, A., Anshakova, A., Malinovskaya, J., Melnikov, P., Baklaushev, V., Chekhonin, V.,
781 Maksimenko, O., Titov, S., Balabanyan, V., Kreuter, J., Gelperina, S., Abbasova, K., 2018.
782 Nanoparticle-based delivery of carbamazepine: A promising approach for the treatment of
783 refractory epilepsy. Int J Pharm 547, 10–23.
784 https://doi.org/https://doi.org/10.1016/j.ijpharm.2018.05.023

785

786